Scatter and Attenuation Correction in SPECT Using Density Maps and Monte Carlo Simulated Scatter Functions

Michael Ljungberg and Sven-Erik Strand

Radiation Physics Department, University of Lund, Sweden

A new scatter and attenuation correction method is presented in which Monte Carlo simulated scatter line-spread functions for different depth and lateral positions are used. A reconstructed emission image is used as an estimate of the source distribution in order to calculate the scatter contribution in the projection data. The scatter contribution is then subtracted from the original projection prior to attenuation correction. The attenuation correction method uses density maps for the attenuation correction of projection data. Simulation studies have been done with a clinically realistic source distribution in cylindrical, homogeneous water phantoms of different sizes and with photon energies corresponding to ^{201}T1, ^{99m}Tc, and ^{111}In. The results show excellent quantitative results with an accuracy within ±10% for most of the source positions and phantom sizes. It has also been shown that the variation in the event distribution within the source region in the images has been significantly decreased and that an enhancement in the contrast has been achieved.

J Nucl Med 1990; 31:1560–1567

Quantitative SPECT studies, based on standard NaI(T1) scintillation camera equipment, today are limited due to photon attenuation and scatter in the object. Due to the complexity of the inherent nature of these effects, particularly when the activity distribution is located in nonhomogeneous regions of the object, no general analytical solution that corrects these effects has yet been reported.

Several attenuation correction methods have been reported and used in clinical studies (*1–7*). These methods all use a single, empirical determined, effective attenuation coefficient to quantitatively take into account the contribution absorbed and scattered photons. The effective attenuation coefficient is generally lower than the narrow-beam attenuation coefficient since the treatment of scatter events in the attenuation correction are not different from the primary events. In nonhomogeneous regions, such as the thoracic region, these methods have limited accuracy. A knowledge of the density distribution is here necessary for a proper attenuation correction, as shown by us earlier (*8*).

It is also essential to take into account the contribution of scatter events in the image. The scatter contribution is an effect of the poor energy resolution of the NaI(T1) scintillation crystal (~10%–15% FWHM at 140 keV), resulting in an ineffective discrimination of scattered photons. Several scatter correction techniques have been described and compared in the literature. These methods can be divided into two major groups.

1. *The Dual-Window technique* that is based on a secondary energy window in the Compton distribution to simultaneously acquire a 'scatter' projection P_{sec} together with the projection P_0 in the ordinary photopeak energy window (*9–12*). By assuming the scatter properties in the two energy windows to be qualitatively equal, the scatter events in the photopeak energy window are removed by scaling the 'scatter' projection by a constant k (0.5 in reference (*9*)) and subtracting the results from the photopeak projection according to:

$$P_p = P_0 - [k \cdot P_{sec}], \qquad (1)$$

   where P_p represents the primary events only.
2. *The Convolution Subtraction technique* is based on the assumption that the scatter distribution in the photopeak energy window can be described by a monoexponential function Q with some amplitude A and rate-of-descent B (*13–14*). The scatter component P_s in the acquired projection P_0 is modeled by a convolution of P_0 with the exponential scatter function Q. A scatter-corrected projection, P_p, is obtained by subtracting the estimated

---

Received Nov. 15, 1989; revision accepted Feb. 28, 1990.

For reprints contact: Michael Ljungberg, PhD, Radiation Physics Department, Lasarettet, S-221 85 Lund, Sweden. E-mail: MLJUNGBERG-@SELDC 52.

scatter distribution P_s from P_0, or:

$$P_p = P_0 - [P_0 \otimes\otimes Q]. \tag{2}$$

In reality, the spatial distribution of the scattered events in the Compton window does not correspond to the distribution in the photopeak window (multiple scattering and large-angle scatter events have a greater probability of being found in the Compton continuum). Furthermore, the method may not be sensitive if the source is at varying depths, since k is constant. An advantage of the dual-window technique is, however, that the general principle is simple and is fast to use if proper hardware equipment for the dual-acquisition mode is available.

The monoexponential function used in the convolution method is, on the other hand, derived for the measurement of the scatter properties in the photopeak window. The scatter function Q does not, however, take into account the source depth. A report has, however, recently been published (*15*) in which a two-exponential scatter function of different amplitudes and slopes (one for superficial activity and one for intermediate activity) has been used.

It is essential for a proper scatter correction to have knowledge both of accurate spatial distribution of scattered photons in the acquired projections and a quantitative estimate of the amount. In this paper, a new scatter correction method is presented that takes into account these requirements by estimating the scatter component in the projection from scatter functions that depends on depth and lateral position of the source. Extensive Monte Carlo simulations have been performed to accurately determine the scatter content in the projection image from point-sources in different phantoms.

DESCRIPTION OF THE DETECTOR SYSTEM

The Monte Carlo simulations in this work were based on a GE-400T (General Electric Corp., Milwaukee, WI) scintillation camera system with a low-energy, general-purpose collimator where the energy resolution was 13% FWHM for 140 keV photons and the intrinsic spatial resolution was 3 mm.

Three cylindrical, homogeneous water phantoms, of height 200 mm and diameters 220 mm, 250 mm and 300 mm, were investigated in the simulation studies. The phantoms were positioned with their central axes parallel to the surface of the collimator. The distance between the upper phantom surface and the lower collimator surface was 10 mm.

MONTE CARLO CODE

The Monte Carlo program used in this work is based on sampling uniformly distributed random numbers to select stochastic processes, e.g., the type of photon interactions and the photon path length, when modeling the history of a photon from beginning to end. The details of the Monte Carlo code have been described elsewhere (*16*). In short, the program works as follows: Radioactive decays are sampled within a defined source volume. The photons emitted from the decays are followed in the phantom. Compton and coherent interactions are simulated according to the relative interaction probabilities for the phantom material. After escaping from the phantom, the photons are followed in the direction towards the scintillation camera. A routine checks whether the photon will pass the collimator. If so, the photons are followed in the scintillation crystal until total absorption or escape.

The centroid of the imparted energy is calculated, together with the total imparted energy for each interaction in the crystal, and defines the apparent position of the event. No explicit simulation of lightguides and photomultiplier tubes (PMTs) is included. Instead, the energy resolution is simulated by convolving the imparted energy with an energy-dependent Gaussian function. If the magnitude of the imparted energy in the crystal at the end of a photo history is within a predefined energy window, the history weight is added to an image matrix in a cell position corresponding to the centroid of the imparted energy.

METHODS

Calculations of Scatter Line-Spread Functions

Simulations of point sources for three different photon energies corresponding to clinically important radionuclides (75 keV for ^{201}Tl, 140 keV for ^{99m}Tc, and 247 keV for ^{111}In), were made for different positions inside the phantoms. In the following text, the name of the radionuclide is used rather than the actual value of the photon energy. The relative position of the point sources in the phantom are indicated in Figure 1 as plus signs. The four scatter line-spread functions (SLSF), shown in Figure 1, are corresponding to the location encircled. The distance between the point sources in both y- and z-direction was 25 mm, 29 mm, and 35 mm for the 220 mm, 250 mm, and 300 mm diameter phantoms, respectively. Due to symmetry, only one projection angle for each phantom was simulated.

The energy window was 30% for ^{201}Tl, 25% for ^{99m}Tc, and ^{111}In. Scatter point-spread projections, $P_s(l,i,j)$, were calculated for those events which originated from photons scattered in the phantom and accepted within the energy window. The indices i and j indicate the cell position in the projection matrix and l is a notation indicating the position of the point source in the phantom. The scatter-to-total fraction $ST(l)$ (the ratio between the number of scatter events and the number of scatter plus primary events) was calculated for each source position. After termination of all photon histories for source position l, the number of events in each pixel in row j in $P_s(l,i,j)$ was integrated along the column i to obtain a scatter line-spread function $SLSF(l,i)$. The scatter LSF or scatter line-spread function was normalized to unity area and stored in a

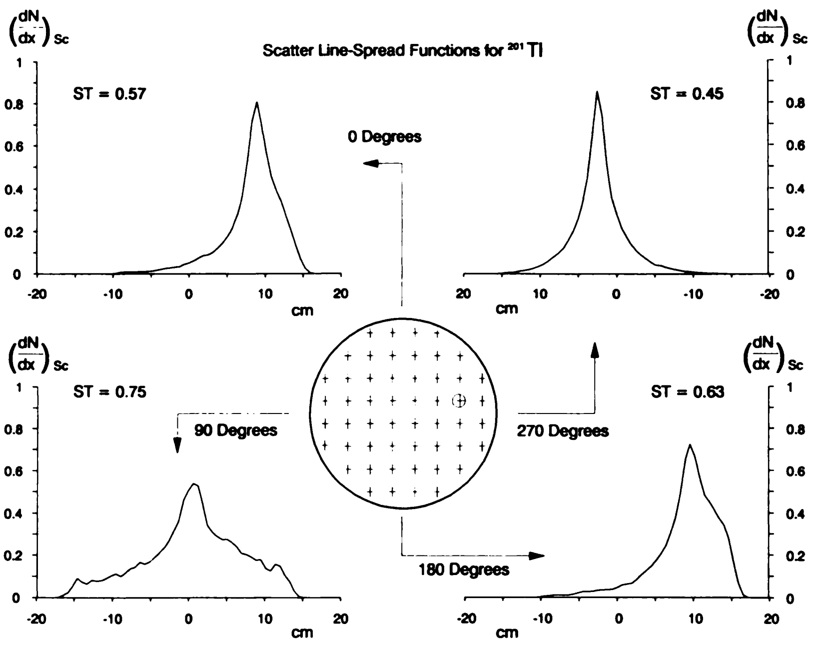

FIGURE 1
The relative positions, denoted as '+,' of the point sources in the phantoms for the calculation of the scatter line-spread functions. Four scatter line-spread functions and scatter-to-total ratios obtained from the location encircled are shown for different projection angles.

data file together with the scatter-to-total fraction $ST(l)$ for the location l of the point source.

Correction for Attenuation

The correction for attenuation is based on using a narrow-beam mass-attenuation coefficient μ/ρ for the object and density maps $\rho(i,j)$ of 64 × 64 cells that describe the density variation of the object. Correction factors, $K(\theta,r)$, are calculated from an uncorrected, reconstructed emission image $E_0(i,j)$, and a density map corresponding to the position of the emission image in the object. Two new projection rays are calculated from the reconstructed emission image $E_0(i,j)$ to estimate $K(\theta,r)$ for a particular projection ray r at an angle θ. The first is an unattenuated projection, calculated by simply summing the pixel contents in the emission image along the ray-of-view $\gamma(\theta,r)$. The second projection is calculated by taking into account the photon attenuation from the location of each pixel to the border along the ray-of-view before summing the pixel contents. The correction factor is obtained by the ratio between these two projections according to the equation:

$$K(\theta,r) = \frac{\sum\limits_{\gamma(\theta,r)} E_0(i,j)}{\sum\limits_{\gamma(\theta,r)} [E_0(i,j)\cdot\exp(-\mu d)]}, \qquad (3)$$

where

$$\mu d = \frac{\mu}{\rho}\cdot\Delta s\cdot\sum_{\gamma(\theta,r)} \rho(i,j) \qquad (4)$$

and $\gamma(\theta,r)$ is the ray-of-view, scanned through the emission image $E_0(i,j)$ for the particular projection angle θ, Δs is the pixel size in the emission map $E_0(i,j)$, and the density map $\rho(i,j)$.

Correction for Scatter

The reconstructed, uncorrected emission image $E_0(i,j)$ of the original projection data $P_o(\theta,r)$ is also used as an estimate of the activity distribution in the object and thus the origin of the scatter component in the projection. The scatter distribution in the projection $P_o(\theta,r)$ from a particular pixel element i,j along a particular ray-of-view $\gamma(\theta,r)$ is calculated for each pixel value by selecting the $SLSF(l,r)$ that is closest to the apparent position of the pixel in the object. The content in the pixel $E_0(i,j)$ is multiplied by the scatter-to-total fraction, $ST(l)$, relevant for the selected scatter LSF, to calculate the fraction scattered photons originated from the location of that particular pixel. The numerical value of $ST(l)$ is obtained by linear interpolation. The spatial distribution in the projection data from the fraction scattered photons is calculated by a 1D-convolution with the scatter LSF according to:

$$P_s(\theta,r) = \sum_{\gamma(\theta,r)} ST(l)\cdot \sum_{\tau=-R}^{R} E_0(i,j)_{\gamma(\theta,r)}\cdot SLSF(l,r-\tau), \qquad (5)$$

where 2R is the width of the projection field and τ is a dummy variable.

Since the activity distribution in the emission image $E_0(i,j)$ does not take into account the photon attenuation as a function of the projection angle θ when the source is off-axis, a normalization factor $\alpha(\theta)$ is calculated according to:

$$\alpha(\theta) = \frac{\sum\limits_{r} P_0(\theta,r)}{\frac{1}{M}\cdot\sum\limits_{r}\sum\limits_{\gamma(\theta,r)} E_0(i,j)} \qquad (6)$$

where M is the number of projection angles in the study.

Total Correction

Projections corrected for attenuation and scatter are obtained from the original projection according to the expression:

$$P_p(\theta,r) = [P_0(\theta,r) - \alpha(\theta)\cdot P_s(\theta,r)]\cdot K(\theta,r). \qquad (7)$$

Equation 7 is applied on all projection rays r and all projection angles θ. The corrected projection $P_p(\theta,r)$ is reconstructed to a quantitatively accurate emission image $E_p(i,j)$.

The calculation of the normalization factor $\alpha(\theta)$ thus corrects the magnitude of $P_s(\theta,r)$ so that there exists a relevant scatter-to-total fraction between the integral of the calculated scatter distribution and the integral of the original projection for the current projection angle.

Phantom Simulations

SPECT studies were simulated using the Monte Carlo program to evaluate the accuracy of the correction method for a clinically realistic source distribution. The dimensions and shape of the source are shown for two different views in Figure 2. Simulations were made with the source at the center (A) of the phantoms and at four different positions (B–E) off-axis. The lateral shifts of the source relative to the center axis for the different phantoms are given in Table 1.

For each source position and radionuclide, projections of 38 mm thickness (six pixels) were simulated for 64 angles in a 360° rotation mode. The positions of the projections are indicated in Figure 2B. The simulated projections were reconstructed by a filtered backprojection program where a Hamming filter was used. The pixel size in the reconstructed image was 6.3 × 6.3 mm^2.

Simulations were also made for the source volume "free in air" where no photon interactions were simulated in order to be used as reference studies for which the results and accuracy of the attenuation and scatter correction were compared. Thus, in these simulations no attenuation and scattering of the photons occurred.

The attenuation correction was applied using a mass-attenuation coefficient of 0.188 cm^{2}g^{-1} for ^{201}Tl, 0.154 cm^{2}g^{-1} for ^{99m}Tc, and 0.128 cm^{2}g^{-1} for ^{111}In (*17*). No averaging of opposite projection data was performed prior to the photon attenuation and scatter correction, in order to increase the accuracy of the correction of the projection data in the studies when the radioactive source distribution was shifted laterally off-axis. Before reconstruction, however, opposite projections were averaged by arithmetical mean since this is more in accordance to the nature of the additative backprojection and that the nonlinear effects from geometrical-mean averaging of the corrected results have not fully been investigated.

TABLE 1
Lateral Displacement of the Source Relative to the Center of the Phantom

	Phantom diameter		
Position	220 mm	250 mm	300 mm
A	0 mm	0 mm	0 mm
B	20 mm	20 mm	30 mm
C	40 mm	50 mm	50 mm
D	50 mm	60 mm	80 mm
E	60 mm	75 mm	100 mm

The uncorrected and corrected emission images were evaluated using six different regions of interest (ROI). The size and relative position of each ROI, shown in Figure 2A, were used for all source positions inside the phantoms.

Absolute Quantification

To evaluate the accuracy of the quantification after correction, the events within ROI$_1$ was compared to the corresponding number of events for the air simulation. The results of both uncorrected and corrected emission images are shown in Figure 3 as the percentage of events relative to the air images. In the figure are given three groups of bars for the three phantoms. Each of the main groups contain five subgroups that correspond to the different displacement of the source. The percentage events-relative-air are shown by bars of different greyshades for each of the three photon energies in these subgroups.

It can be seen in Figure 3A that the attenuation is between 60% to 90% in the simulation studies. When the source is positioned off-axis the magnitude of the attenuation decreases. The attenuation effect is most marked for the photons with the lowest energy. In addition, the difference in photon attenuation for the three energies seems to be largest when the source is at the center of the phantom and decreases when it is moved laterally off-axis.

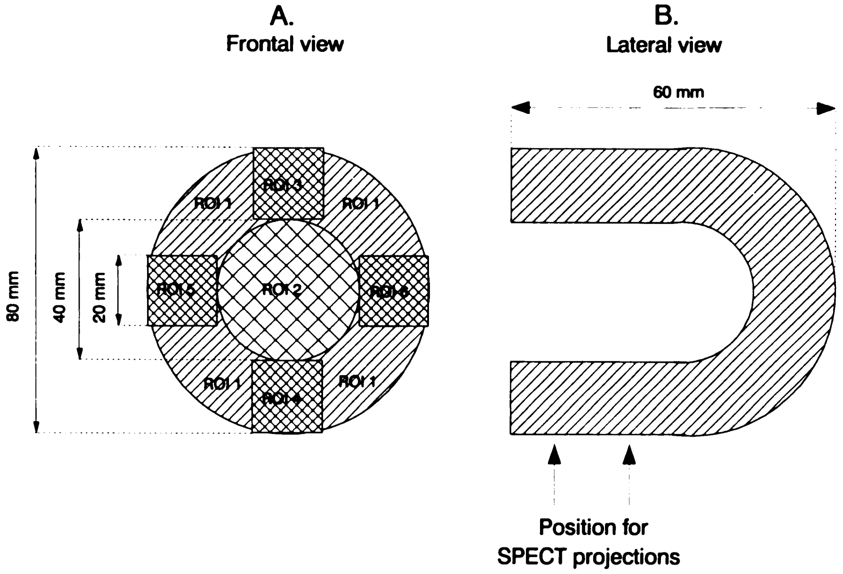
A.
Frontal view

B.
Lateral view

FIGURE 2
The shape and dimension of the simulated source phantom are shown in two views. The evaluated regions of interest ROI$_{1-6}$ are indicated.

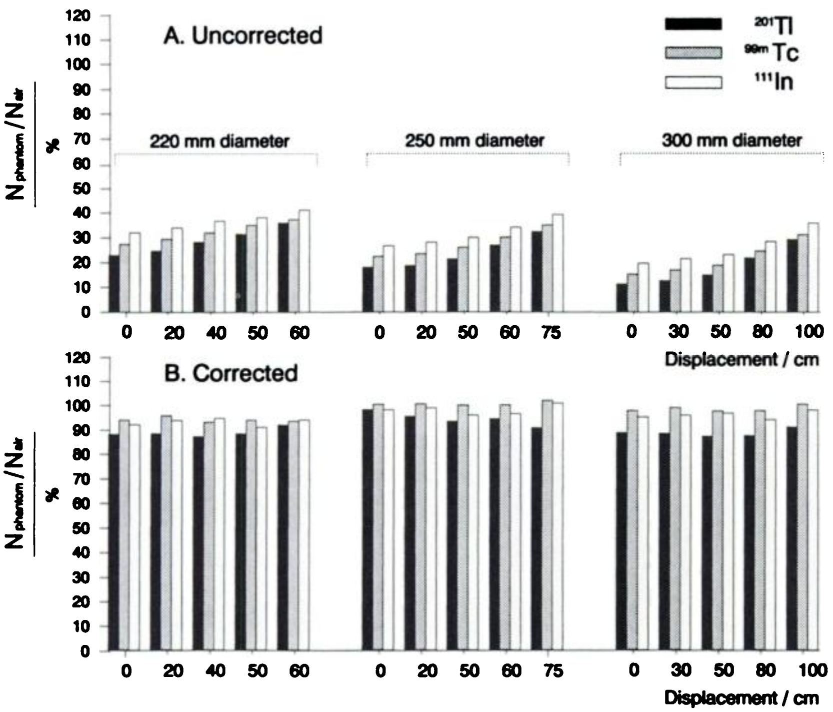

FIGURE 3
The events in ROI_1 for uncorrected and corrected images relative to the events in ROI_1 for the air images.

The corresponding data for images corrected for both attenuation and scatter are shown in Figure 3B. The results show an overall good correction within the whole phantom. The quantitative values are for most of the cases in a range within 10%, when compared with the air simulation. For the 220-mm phantom, the results tend to be undercorrected for all photon energies and phantom sizes. There is a slight undercorrection for ^{201}Tl that, for the different source positions, has an average percentage of events-relative-air of 88%. For ^{99m}Tc and ^{111}In, the corresponding average values are 94% and 93%, respectively. For the 250-mm phantom, the corrected values have an excellent accuracy. In this case, the average values are 94% for ^{201}Tl, 100% for ^{99m}Tc, and 98% for ^{111}In. For the 300-mm phantom, the correction is also of high accuracy, with values for ^{99m}Tc of 98% and ^{111}In 95%. For this phantom size also values for ^{201}Tl are slightly undercorrected, with an average value of 88%. There is no dependence on the source position or phantom size as is the case of the uncorrected values, which indicates that the correction method takes into account these parameters.

Event Distribution

To investigate the spatial distribution of events, four small square ROIs, ROI_{3-6}, were defined symmetrically within the larger ROI_1, (Fig. 2A). The percentage difference in number of events, defined as the [(max-min)/mean] for the four ROIs, was calculated for both uncorrected and corrected images.

In Figure 4A is shown a bar diagram of the relative difference for the uncorrected images. The diagram is similar to the one in the previous section. It can be seen that there is an increasing difference between the number of events in ROI_{3-6} when the source is positioned near the phantom surface. This is especially evident for ^{201}Tl. In the central position no significant deviation as a function of the photon energy can be seen. This can be explained by the fact that both the phantom and the source are symmetrical and homogeneous in shape. It can also be seen that near the phantom surface the deviation decreases with higher photon energies.

Figure 4B shows the corresponding results for the emission images corrected for the photon attenuation and scatter. It can now be seen that the magnitude of the relative difference between the ROIs for the different source positions has been decreased radically.

Contrast

The contribution from scattered photons results in events appearing in regions in the emission images that correspond to locations in the object where no activity really exists. For example, region 2 (see Fig. 2A) in the emission images should ideally contain no events since no radioactivity exists in the corresponding volume in the phantom, as is indicated in Figure 2B. The unwanted scatter contribution in this region can be described by the contrast, defined in this work as:

$$C = 1 - \left[\frac{N_2/n_2}{N_1/n_1}\right], \tag{8}$$

where N_i is the number of events in the particular region and n_i is the number of pixel elements.

Figure 5 shows tomographic images for the ^{201}Tl source placed in position D in the 300-mm diameter phantom. A vertical profile through the distribution is shown in Figure 5. It can be seen that there is good agreement between the profile through the corrected image and the profile from the air simulation. The misplacement of events has decreased significantly and the contrast enhanced.

The contrast between region ROI_1 and ROI_2 has been evaluated and the average percentages for the different phantoms and radionuclides have been calculated. As can be seen

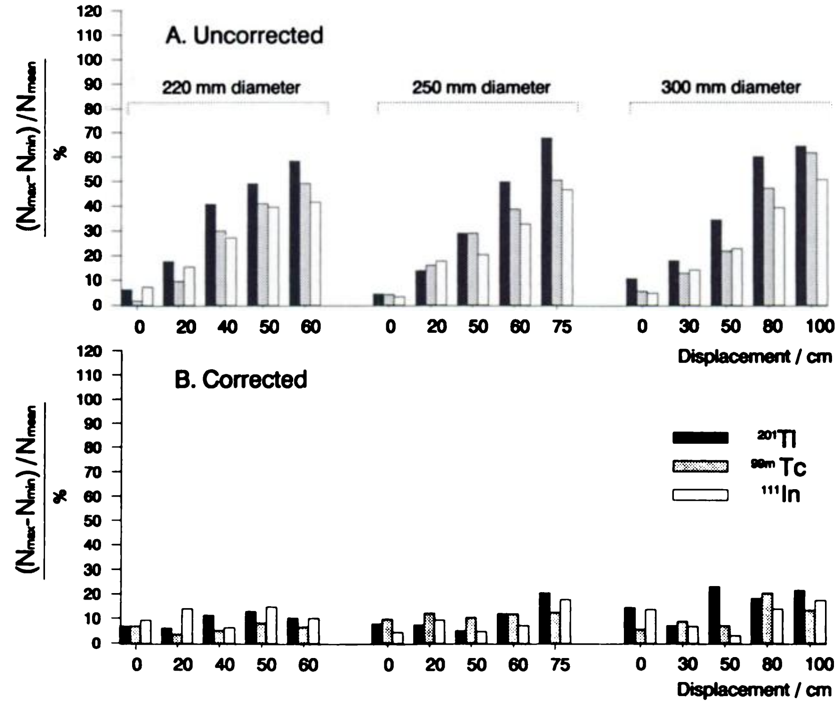

FIGURE 4
The relative difference [(max-min)/mean] in number of events in ROI_{3-6}.

from Figure 6, contrast enhancement has been achieved after correction for attenuation and scatter. The values now correspond more to the "true" contrast of air simulations. Note that the contrast of the air simulation is not zero despite the fact that ROI_2 contains no radioactivity. The magnitude of the contrast is instead within a range of 70%–80%, which is mainly a result of the spatial resolution of the detector system (mainly the collimator resolution). There will, thus, be a spillover of events from ROI_1 into ROI_2 that is not caused by the contribution from scattered photons.

DISCUSSION AND CONCLUSION

A new method has been described that corrects SPECT projection data for both the photon attenuation and contribution from scattered photons. Our results show that quantitative SPECT information within ± 10% can be achieved with high accuracy in both the central part of the phantom and near the surface for both ^{99m}Tc and ^{111}In. For ^{201}Tl, however, the simulations indicate a slight underestimation of ~10% for the 220-mm phantom and the 300-mm phantom. Further work must be done to evaluate the cause of this undercorrection. It has also been demonstrated that the average contrast in the corrected images for the different source positions has been increased to the contrast level of the corresponding air simulation.

An accurate spatial distribution of events within a region of interest is essential even if quantitative measurements are of less importance. This has been demonstrated in Figures 4 and 5. The cause of the difference in the distribution of events in Figure 4 is mainly the photon attenuation and implies that even for a relatively small source distribution (a diameter of 80 mm in this work) significant artefacts in the image may be introduced if a proper correction for the attenuation and scatter contribution is not achieved. This is especially true for low-energy photon emitters, such as ^{201}Tl. There is thus a possibility that the reduction of events in a portion of the source volume could be misinterpreted as a lower activity uptake. This indicates that correction for attenuation and scatter is important even for qualitative studies for which only 'relative' estimations of activity or 'evaluation by viewing' is of interest.

The scatter correction technique described here is based on estimating a scatter distribution by a one-dimensional convolution where simulated, two-dimensional scatter functions were used. The scatter functions have been determined for different depths and lateral positions in cylindrical, homogeneous water phantoms. No assumption is made that the scatter function can be described by a certain analytical expression. Instead, the scatter functions consist of tabulated numerical values. This has the advantage that the correction method allows any kind of scatter function shape to be used. Preliminary results indicate (*18,19*) that in nonhomogeneous regions, such as the thoracic region, the scatter function deviates substantially from the commonly used assumption of a monoexponential shape. It may, thus, be possible to simulate accurate scatter functions for nonhomogeneous objects, allowing proper scatter correction in a region with large variation in density.

We believe that the Monte Carlo method is a very useful complement to measurements since it offers the

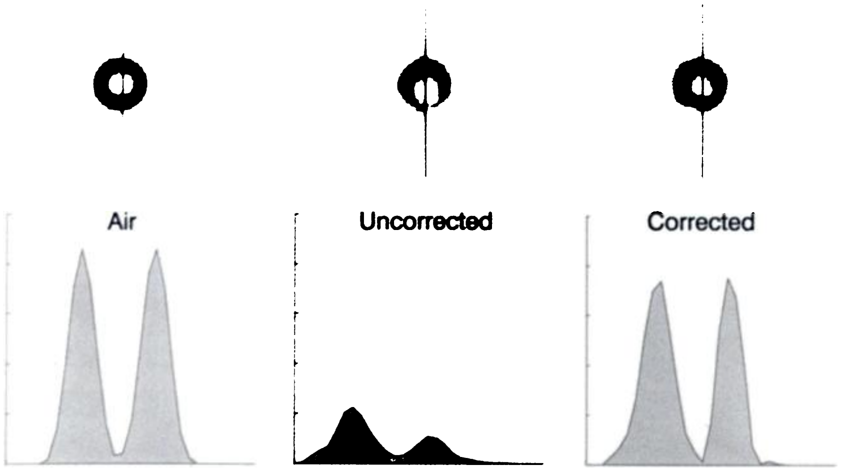

FIGURE 5
Tomographic images and vertical profiles for uncorrected, corrected and air images corresponding to a source of ^{201}Tl in position D in the 300-mm water phantom.

possibility to both quantitatively and qualitatively determine the amount of primary and scatter events in the images and relate this to air simulation of extended sources. Further evaluations of both measured and simulated projection data of different kinds of sources (shapes and sizes) must be made in order to fully investigate the accuracy of the estimated scatter component in the images from the tabulated scatter LSFs. For example, if the size of the source is small then an overestimation in the scatter component in the projection may be expected since the scatter line spread functions probably will predict to much scatter.

An accurate correction method for photon attenuation in addition to an effective scatter correction (*8,20–22*) is essential for quantitative SPECT. The correction method described in this work is based on a method using density maps of the object. The maps can be simulated, measured by an external flood source measurement or obtained by x-ray computed tomography. The outline of the object is accurately defined since the density values outside the boundary are very close to zero. Recent studies have shown a high degree of accuracy of the quantification of activity contents in line sources of ^{201}Tl, ^{99m}Tc, and ^{111}In in different positions in a nonhomogeneous Alderson phantom.

As a conclusion, it should be pointed out that there are several advantages to be gained from the accurate quantitative measurement with SPECT equipment, both for contrast enhancement in diagnostic imaging and for calculation of organ doses in radionuclide therapy applications. The results presented here have been encouraging and further work will focus on implementing nonhomogeneous scatter and attenuation corrections and thus making the algorithm attractive for clinical use, for example for myocardial studies with ^{201}Tl.

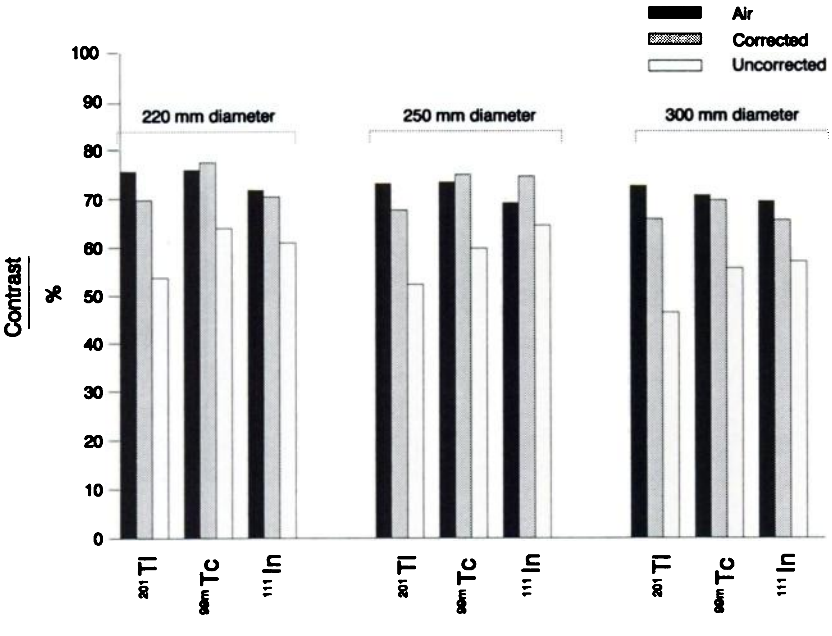

FIGURE 6
The contrast in the tomographic images between ROI$_1$ and ROI$_2$.

APPENDIX

Summary of Symbols

P_0	Uncorrected original projection of primary and scattered photons
P_p	Projection representing primary photons only
P_s	Projection representing scattered photons only
E_0	Reconstructed uncorrected image
E_p	Reconstructed corrected image
l	Point-source location for the scatter line-spread function
r	Position of projection ray in the projection set
θ	Projection angle
$K(\theta,r)$	Attenuation correction factor
$SLSF(l,r)$	Scatter line-spread distribution
$ST(l)$	Scatter-to-total ratio
$\alpha(\theta)$	Normalization factor for the calculated scatter projection
μ/ρ	Narrow-beam mass-attenuation coefficient
$\rho(i,j)$	Matrix describing the density distribution of the object
$\gamma(\theta,r)$	Current ray-of-view when scanning through, for instance, the emission image $E_0(i,j)$
Δs	Pixel size for the emission image and the density map

ACKNOWLEDGMENTS

This work has been supported by grants from the Swedish Cancer Foundation, grant no. 2353-B87-01XA and no. 2353-B89-03XA; the John and Augusta Person's Foundation for Scientific Research, Lund; The Royal Physiographic Society, Lund; the Medical Faculty of Lund; and Mrs Bertha Kamprad's Cancer Foundation.

REFERENCES

1. Budinger TF, Gullberg GT, Huesman RH. Emission computed tomography. In: Herman GT, ed. *Image reconstruction from projections: implementation and applications.* New York: Springer Verlag; 1979:147–246.
2. Chang LT. A method for attenuation correction in radionuclide computed tomography. *IEEE Trans Nucl Sci* 1978; NS-25:638–643.
3. Larsson SA. Gamma camera emission tomography: development and properties of a multi-sectional emission computed tomography system. *Acta Radiologica Suppl* 1980; 363:1–75.
4. Walters TE, Simon W, Chesler DA, et al. Attenuation correction in gamma camera computed tomography. *J Comput Assist Tomogr* 1981; 5:89–94.
5. Soussaline FP, Cao A, LeCoq G, et al. An analytical approach to the single photon emission computed tomography with attenuation effect. *Eur J Nucl Med* 1982; 7:487–493.
6. Mukai T, Links J, Douglass K, et al. Scatter correction in SPECT using non-uniform attenuation data. *Phys Med Biol* 1988; 33:1129–1140.
7. Mas J, Younes RB, Bidet R. Improvement of quantification in SPECT studies by scatter and attenuation compensation. *Eur J Nucl Med* 1989; 15:351–356.
8. Ljungberg M, Strand S-E. Attenuation correction in SPECT based on transmission studies and Monte Carlo simulations of build-up functions. *J Nucl Med* 1990; 31:493–500.
9. Jaszczak RJ, Greer KL, Floyd CE, et al. Improved SPECT quantification using compensation for scatter photons. *J Nucl Med* 1984; 25:893–900.
10. Koral KF, Clinthorne NH, Rogers WL. Improving emission computed tomography quantification by Compton scatter rejection through offset windows. *Nucl Inst Meth in Phys Res* 1986; A242:610–614.
11. Yanch JC, Irvine AT, Webb S, et al. A comparison of deconvolution and windowed subtraction techniques for scatter compensation in SPECT. *IEEE Trans Med Imag* 1988; 7:13–20.
12. Gilardi MC, Bettinardi V, Todd-Pokropek A, et al. Assessment and comparison of three scatter correction techniques in single photon emission computed tomography. *J Nucl Med* 1988; 29:1971–1979.
13. Axelsson B, Msaki P, Israelsson A. Subtraction of Compton-scattered photons in single-photon emission computed tomography. *J Nucl Med* 1984; 25:490–494.
14. Msaki P, Axelsson B, Dahl CM, et al. Generalized scatter correction in SPECT using point scatter distribution functions. *J Nucl Med* 1987; 28:1861–1869.
15. Msaki P, Axelsson B, Larsson SA. Some physical factors influencing the accuracy of convolution scatter correction in SPECT. *Phys Med Biol* 1989; 34:283–298.
16. Ljungberg M, Strand S-E. A Monte Carlo program for the simulation of scintillation camera characteristics. *Comput Meth Prog Biomed* 1989; 29:257–272.
17. Berger MJ, Hubbell JH. XCOM: photon cross sections on a personal computer. *National Bureau of Standards* 1987; NBSIR 87-3597.
18. Ljungberg M, Strand S-E. Monte Carlo simulated scatter function for non-homogeneous objects. *Med Phys* 1989; 16:463 (F6).
19. Ivanovic M, Weber DA. Evaluation of Compton scatter distribution function in nonuniform attenuation media [Abstract]. *J Nucl Med* 1989; 30:875.
20. Manglos SH, Jaszczak RJ, Floyd CE, et al. Nonisotropic attenuation in SPECT: phantom test of quantitative effects and compensation techniques. *J Nucl Med* 1987; 28:1684–1691.
21. Bailey DL, Hutton BF, Walker PJ. Improved SPECT using simultaneous emission and transmission tomography. *J Nucl Med* 1987; 28:844–851.
22. Tsui BMW, Gullberg GT, Edgerton ER, et al. Correction of nonuniform attenuation in cardiac SPECT imaging. *J Nucl Med* 1989; 30:497–507.